# StereoCrafter-Zero: Zero-Shot Stereo Video Generation with Noisy Restart

Jian Shi Qian Wang Zhenyu Li Ramzi Idoughi Peter Wonka King Abdullah University of Science and Technology, Thuwal, Saudi Arabia {jian.shi, qian.wang, zhenyu.li.1, ramzi.idoughi, peter.wonka}@kaust.edu.sa



Figure 1. With just a single image and an associated text prompt (left), our method generates compelling stereo video sequences. The analyph visualization (right) offers an intuitive way to perceive the stereoscopic effects, showcasing the power of our approach.

# **Abstract**

Generating high-quality stereo videos that mimic human binocular vision requires consistent depth perception and temporal coherence across frames. Despite advances in image and video synthesis using diffusion models, producing high-quality stereo videos remains a challenging task due to the difficulty of maintaining consistent temporal and spatial coherence between left and right views. We introduce StereoCrafter-Zero, a novel framework for zeroshot stereo video generation that leverages video diffusion priors without requiring paired training data. Our key innovations include a noisy restart strategy to initialize stereo-aware latent representations and an iterative refinement process that progressively harmonizes the latent space, addressing issues like temporal flickering and view inconsistencies. In addition, we propose the use of dissolved depth maps to streamline latent space operations by reducing high-frequency depth information. Our comprehensive evaluations, including quantitative metrics and user studies, demonstrate that StereoCrafter-Zero produces

high-quality stereo videos with enhanced depth consistency and temporal smoothness, even when depth estimations are imperfect. Our framework is robust and adaptable across various diffusion models, setting a new benchmark for zeroshot stereo video generation and enabling more immersive visual experiences. Our code is in https://github.com/shijianjian/StereoCrafter-Zero.

### 1. Introduction

The resurgence of head-mounted displays has renewed interest in stereo images and videos. Stereo image conversion, which aims to reconstruct stereo pairs from single images, has progressed significantly. However, inconsistent depth information can cause visual artifacts and incoherence between frames, undermining the immersive experience that stereo videos are intended to provide. Previous works [27, 31, 35, 38, 39] have improved depth consistency and parallax effects in stereo image generation. Recent studies have extended stereo conversion techniques to video, emphasizing the importance of temporal consistency

to produce smooth and coherent stereo video sequences [29, 48]. Meanwhile, diffusion models have emerged as a powerful paradigm for generative tasks, demonstrating remarkable proficiency in capturing complex data distributions and creating high-fidelity images and videos [13, 26, 28]. Notably, StereoDiffusion [36] demonstrated the potential of zero-shot stereo image generation using diffusion models.

In this work, we explore the relatively unexplored field of stereo video generation with diffusion models in a zero-shot manner without significant computational requirements. Generating stereo video is more complex than generating stereo images, requiring meticulous handling of depth cues to produce realistic parallax and consistent depth perception in both views [3]. Recently, video depth estimation models have improved temporal consistency by accurately capturing and maintaining depth information across video frames [9, 14, 17, 21]. However, for stereo video generation, the core issue lies in the nuanced interplay between depth consistency and temporal coherence, requiring models to maintain consistency both across consecutive frames (temporal consistency) and between the left and right views within each frame (inter-view consistency). Current video generation models primarily focus on overall visual fidelity and temporal smoothness without explicitly enforcing depth consistency between stereo views over time. Thus, existing methods lack mechanisms to dynamically adapt depth information during the diffusion process, which is necessary to accurately represent scene dynamics in stereo video generation.

To address these challenges, we introduce a novel framework for zero-shot stereo video generation that leverages video diffusion priors to generate high-quality stereo videos without the need for paired training data. Instead of performing stereo conversion on the video level, we improve and refine the consistency within the latent features of a video diffusion model. One significant advantage is that our method does not require precise disparity maps. We introduce the concept of dissolved depth maps, which retain only the low-frequency structural depth information. By emphasizing global structure over pixel-level depth variations, our approach reduces high-frequency noise that can lead to misalignment and artifacts in the generated right view. Furthermore, our approach seamlessly integrates advanced video depth estimation into the diffusion-based synthesis process, ensuring both depth consistency and temporal coherence. Our main contributions are as follows:

- We introduce **StereoCrafter-Zero**, a novel approach for zero-shot stereo video generation based on video diffusion models without the need for paired training data.
- To enhance latent consistency, we employ a noisy restart strategy to obtain stereo-aware initial latents, followed by an iterative refinement process that systematically injects controlled noise into the diffusion process, progressively

- improving the harmony of the latent space.
- We introduce dissolved depth maps, a novel depth representation that retains only low-frequency structural depth, reducing high-frequency noise and improving stereo coherence. Our approach avoids reliance on accurate depth estimation, making the approach more robust.
- We conduct thorough evaluations, including statistical analysis and user studies, demonstrating the ability of our method to generate high-quality stereo videos.

# 2. Related Works

# 2.1. Novel-View Synthesis

Novel-view synthesis task aims to generate images from new camera perspectives based on one or more source images. Recent novel-view synthesis works such as [19, 20, 33, 34, 43, 44] demonstrate good results in creating a stereo pair of a given scene. However, these methods require scene-specific optimization, limiting their applicability to video data. Another category of approaches [11, 32, 46] employs the depth-warping technique to synthesize novel views and subsequently refines the warped images. These approaches suffer from visual artifacts in the inpainted regions, particularly in complex scenes with large disparities or occlusions. More importantly, these methods cannot enforce temporal consistency, which is an important requirement for handling video-based novel view synthesis. The Collaborative Video Diffusion (CVD) technique [18] utilized a cross-video synchronization module to directly generate multi-view videos for predefined camera trajectories. Another line of work [2, 42, 45] focuses on explicit 3D scene construction with temporal dynamics, enabling the generation of novel-view videos. However, these methods are limited to simple object-centric scenes and exhibit limited visual quality when applied to complex scenes. Generating novel-view videos with complex visual content remains an open challenge.

### 2.2. Stereo Content Generation

Stereo content generation has evolved significantly from traditional disparity estimation and view synthesis methods to modern deep learning approaches that enhance both depth accuracy and visual realism. Early approaches [35, 39] utilized neural networks and generative networks to predict disparity maps and synthesize corresponding views, enabling the generation of stereo image pairs. Recent advancements have extended these techniques to video by incorporating temporal coherence, thereby creating smooth and immersive stereo video sequences [29, 47, 48]. Additionally, diffusion models have been successfully adapted for stereo image generation, enabling zero-shot synthesis [36]. However, the application of such zero-shot generative models for stereo video remains under exploration

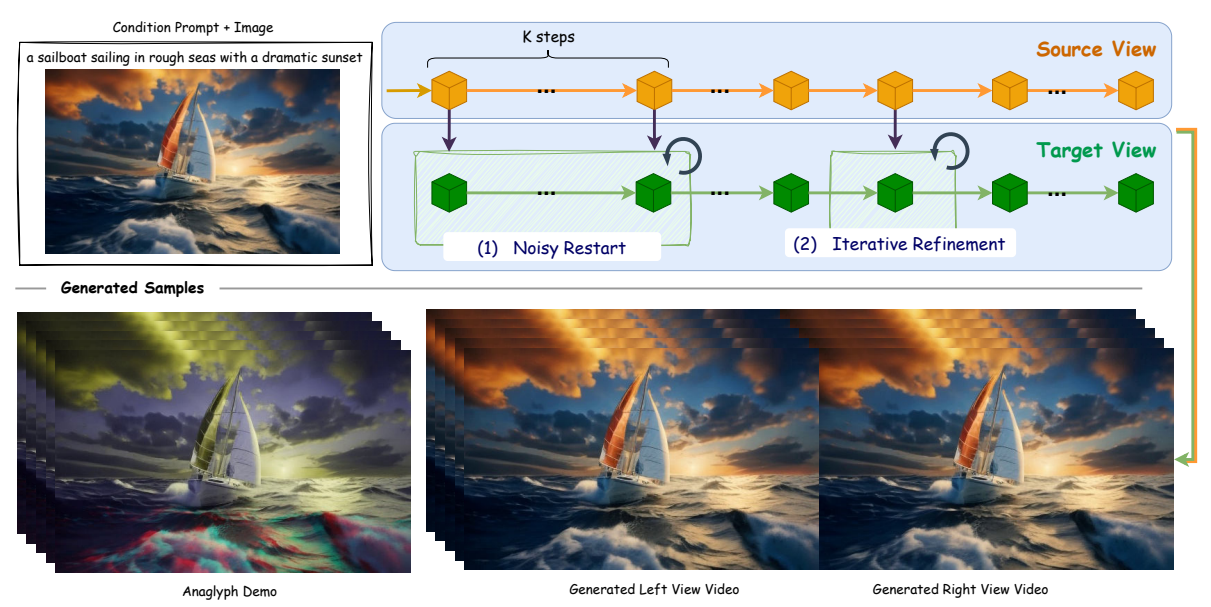


Figure 2. An overview of the *StereoCrafter-Zero* pipeline. Top: Our method is based on two main components: (1) **Noisy Restart** for a robust initial latent estimation (Sec. 3.1) and (2) **Iterative Refinement** for the latent refinement (Sec. 3.2) during the sampling step. Bottom: The proposed pipeline takes a conditioning image and text prompt as input, generating both left and right views that produce a strong stereoscopic effect.

due to the additional challenges of ensuring both spatial depth fidelity and temporal consistency across frames. A concurrent work [12] proposes a *frame matrix* approach, which involves placing multiple camera views and warping the latent space on every DDIM sampling step. In contrast, our method generates new viewpoints without the need for warping at every step, which significantly reduces the computational costs.

# 3. Method

In this section, we describe the StereoCrafter-Zero framework for zero-shot stereo video generation, which leverages video diffusion priors to synthesize stereo-consistent videos. Let  $\mathbf{X} = \{x_T, x_{T-1}, \dots, x_0\}$  denote the DDIM latent sequence from a video diffusion model with T diffusion steps (e.g., T=50 ). Each latent  $x_t \in \mathbb{R}^{B \times C \times T \times H \times W}$ is a five-dimensional tensor representing a batch of video frames, where B is the batch size, C the number of channels, T the temporal dimension (number of frames), and Hand W the spatial height and width, respectively. By decoding  $x_0$ , we obtain a video sequence  $V \in \mathbb{R}^{B \times 3 \times T \times H' \times W'}$ where H' and W' are the corresponding height and width of the decoded videos. To capture the scene geometry and enable accurate latent warping, we generate depth maps  $\mathbf{D} \in \mathbb{R}^{B \times T \times H' \times W'}$ , which provide per-pixel, temporally consistent depth information. Using these depth maps, the latent features are warped to achieve stereo consistency and account for parallax effects. Let  $\Delta$  denote the disparity map that is computed by Eq. (6), which represents the horizontal shift between the left and right stereo views. The warp operation  $\mathbf{W}(x,\Delta)$  defined in Eq. (7), is then applied to produce the warped latent representation  $x_t^{\mathrm{warp}} = \mathbf{W}(x_t,\Delta)$ . Details of our efficient implementation of the warping algorithm are provided in the *supplementary material*. This warping aligns the latent representations according to depth-induced disparities, which is essential for generating realistic stereo views. The warping process, however, introduces blank regions  $x^{blank} \in \mathbb{R}^{B \times C \times T \times H \times W}$  in the warped latents due to occlusions or disocclusions, defined as:

$$x_t^{blank} = 1$$
 if  $x_t^{warp}$  is undefined, 0 otherwise. (1)

With the aid of a disparity map, each latent feature can be decomposed into  $x_t^{blank}$  and  $x_t^{warp}$  after warping. Maintaining consistency between these two latent parts is critical for creating meaningful and harmonized outputs for each individual view with correct depth cues. Since  $\epsilon_t$  is the only source of randomness during the diffusion process  $referto\ Eq.\ (8)$ , we, therefore, refine the latent features by iteratively injecting  $\epsilon_t$  into the diffusion process.

The main contribution of our paper lies in improving consistency between  $x_t^{blank}$  and  $x_t^{warp}$ . We achieve this through two key steps: (1) **Noisy Restart** (Sec. 3.1), which initializes a reasonable  $x^{blank}$ , and (2) **Iterative Refinement** (Sec. 3.2) that improves the consistency between  $x^{blank}$  and  $x^{warp}$ . In addition, we introduce **Dissolved Depth Maps** (Sec. 3.3) which transform depth maps into lower-frequency representations to enhance the consistency of warped latents with the video diffusion prior.

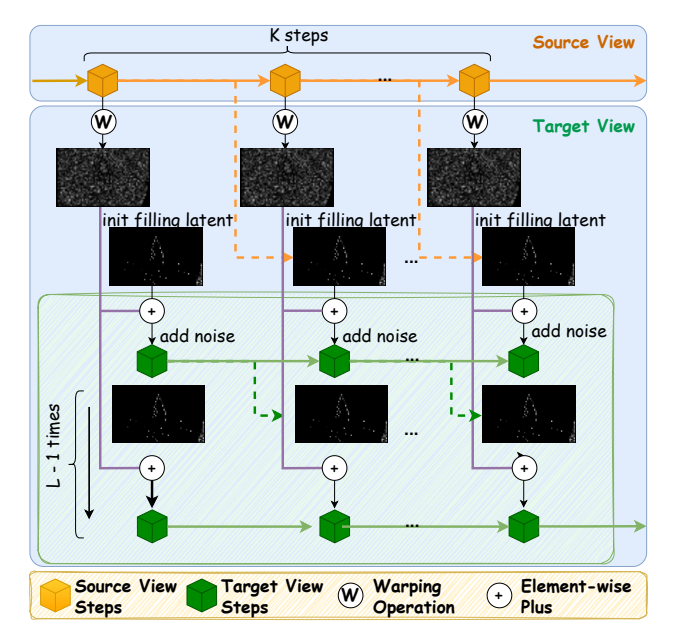


Figure 3. Illustration of the noisy start strategy. At selected steps, we replace the target view sampling with a warped source view. Occluded/disoccluded areas are then filled using the non-warped source view latent, with added noise injected into the latent space. Subsequent iterations update the latents with values from the preceding iteration, while preserving the non-occluded regions.

## 3.1. Noisy Restart

The noisy restart mechanism operates over K diffusion steps for L iterations. We denote the K diffusion steps as  $\{x_t\}_{t=0}^K$ , where  $x_t$  represents the latent state at step t. While K can be a set of discrete timesteps, we use  $K = \{49, ..., 45\}$  in our implementation. The main purpouse of the noisy restart is to introduce random noise into the latent space to prevent structural repetition and ensure smooth transitions. In the first iteration, K filling latents are generated for each diffusion step, while the subsequent iterations will refine the obtained K latents. Referring to Eq. (8), a random noise  $\epsilon_t$  is introduced at each sampling step. If each iteration uses different noise values, consistency across iterations can be disrupted. To address this issue, we initialize fixed noise tensors  $\epsilon'_t$  before starting the diffusion sampling sequence and use the same random seed for each iteration. This operation ensures that the random generator status remains the same across multiple iterations, and the noise injection is controlled solely by  $\epsilon'_t$  and  $\alpha_t$  in Eq. (2). Meanwhile, such a controlled approach promotes structural stability throughout the generation process, ensuring consistent low-frequency noise that preserves major features across frames. We showcase the effectiveness of this method in Sec. 4.

In our work, we use a total of L=7 iterations, with the first iteration directly using the left-view latents as the filling latents. Noise is injected into the latent state through a

weighted addition, balancing the contributions of the existing latent and the injected noise. The update equation for  $x_{t-1}$  is given by:

$$x_{t-1} = x_t \cdot (1 - \alpha_t) + \sigma_t \epsilon'_t \alpha_t \tag{2}$$

where  $\sigma_t$  is the noise magnitude for each timestep, scaling the impact of injected noise, and  $\alpha_t$  is the balancing coefficient controlling the mix between the latent state and the noise. By having noisy restart implemented, the stereoscopic effects can be significantly enhanced, as shown in Fig. 8.

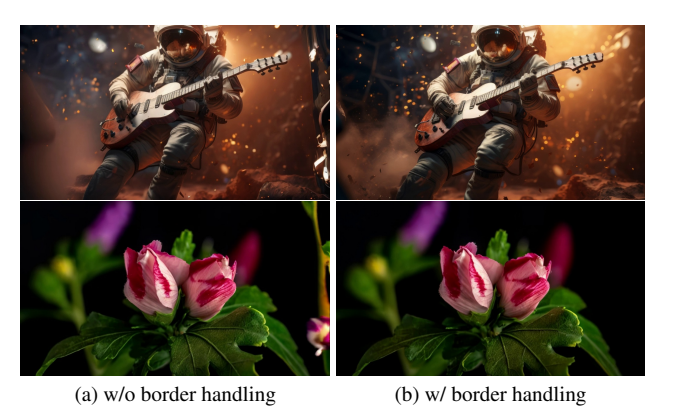


Figure 4. Abrupt border handling. (Left) Images with noticeable abrupt artifacts along the right edge. (Right) Images with border artifacts effectively removed using our method.

Abrupt Border Handling Direct warping of the right view can result in blank regions along the right border. These blank areas may create irrelevant or distracting content in the border regions during the iterative process. To address this issue, we introduce a border-cleaning function that selectively masks and fills these regions using information from the left view, ensuring visual coherence. A border mask,  $M_{\rm border}$ , is created using a heuristic function to select the border areas. We then inpaint these areas with the corresponding regions in the left-view latents, denoted as  $L_l$ . The resulting border refined latent  $L_{r,\rm refined}$  is defined as:

$$L_{r,\text{refined}} = L_r \cdot (1 - M_{\text{border}}) + L_l \cdot M_{\text{border}}.$$
 (3)

This operation replaces the blank columns in the right view with the content from the left view, ensuring visual continuity and eliminating distracting artifacts. This border-cleaning step significantly enhances the coherence of the generated stereo image, particularly by maintaining consistency at the edges of the views. A qualitative evaluation of this technique is presented in Fig. 4.

### 3.2. Iterative Refinement

Since the noisy restart happens on the first several sampling steps, the stereo effects can be shaky and unstable across

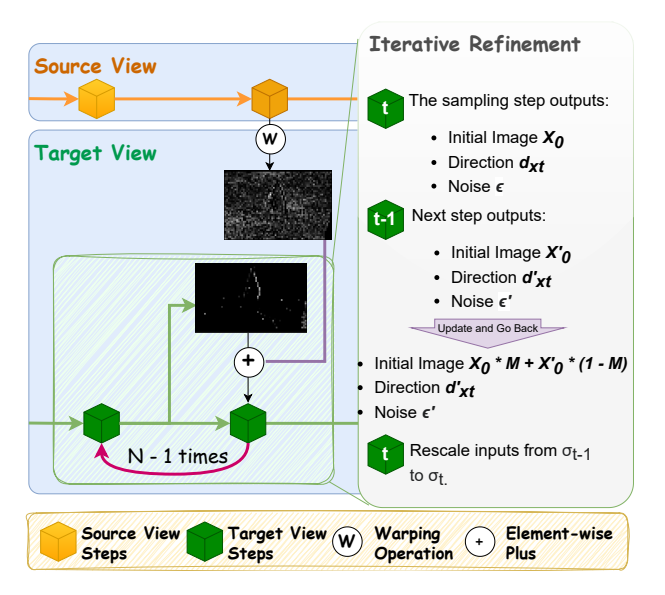


Figure 5. Illustration of the iterative refinement strategy. This process iteratively refine occluded areas within the predicted  $x_0$ . The initial iteration uses standard sampling process. Starting from the second iteration, a new predicted latent is computed and rescaled before each subsequent step.

different timeframes. We hereby propose iterative refinement to stabilize the stereo effects for the later sampling stages. The iterative refinement is achieved by repeating the denoising operation at specific sampling steps. During these steps, the model performs multiple iterations to progressively enhance the latent representation. Since the diffusion model is not inherently aware of stereo effects, this mechanism enables the model to focus on refining details and correcting errors introduced by the video diffusion priors in the later steps.

The iterative refinement process is encapsulated in a loop that performs key operations for each propagation step j within the total number of refinement iterations. Each iteration produces the predicted clean latent  $\hat{x}_0^j$ , scaling factors  $\sqrt{\bar{\alpha}}^j$ , directional term  $d^j$ , noise  $\epsilon^j$ , and the latent  $x_t^j$  for the next iteration. Starting from the second iteration j>1, we update the filling area with the following equation:

$$\hat{x}_{0}^{\prime j} = \begin{cases} \hat{x}_{0}^{\prime j} * \sqrt{\alpha_{t}} + \hat{x}_{0}^{\prime j-1} * (1 - \sqrt{\alpha_{t}}) & \text{if } x_{t}^{blank} = 1, \\ \hat{x}_{0}^{\prime j-1} & \text{otherwise.} \end{cases}$$
(4)

# 3.3. Dissolved (Low-Frequency) Depth Maps

Depth estimation models are typically designed to capture fine, detailed depth information. However, when warping the latent space of a diffusion model, these high-frequency details can compromise the latent space consistency. As shown in Sec. 4.3, high-precision depth maps often introduce artifacts, such as ghosting, during the warping process. We suspect that these fine-grained warping interfere with

temporal coherence, making them less compatible with the video diffusion priors.

To address this issue, we propose a depth-dissolving technique that transforms the depth maps into a lower-frequency representation. Inspired by Dissolving Is Amplifying (DIA) [30], we generate **dissolved depth maps** by leveraging the inherent properties of diffusion models to act as a low-pass filter on the latent space. Using a diffusion-based depth estimation model, we first obtain a depth latent  $x_T$  at the final diffusion step T. Instead of performing a full reverse diffusion process, we excute a single-step reverse diffusion on  $x_T$ . This approximation is designed to suppress high-frequency details, thereby reducing noise and artifacts in the latent representation. Formally, we denote the approximated initial state as  $\hat{x}_{t\to 0}$ , which depends on the selected time step t. The process is defined as follows:

$$\hat{x}_{t\to 0} = \sqrt{\frac{1}{\bar{\alpha}_t}} \cdot x - \sqrt{\frac{1}{\bar{\alpha}_t} - 1} \cdot \epsilon_{\theta}(x, t), \tag{5}$$

where  $\bar{\alpha}_t$  represents the cumulative product of the diffusion coefficients up to time t,  $\epsilon_{\theta}$  is the predicted noise at time t. By emphasizing global structure over pixel-level depth variations, our approach enables smoother disparity transitions. As a result, the warped latents maintain better temporal coherence and align more effectively with the video diffusion priors. Experimental results confirm our hypothesis that dissolved depth maps reduce artifacts such as ghosting and staircase effects.

### 4. Experiments

#### 4.1. Implementation details

We implement our method based on DynamiCrafter [40], a state-of-the-art diffusion-based video generation framework. We also evaluated our method with other diffusion-based video generation methods, such as LDM, in our supplementary material. We infer video depth maps using DepthCrafter [14]. we apply the cross-view attention mechanism on all sampling steps apart from the cross-attention between the latents and the conditions. We use L=7 for noisy restart from t=49 to t=45. Afterward, warping is performed to update the side-view latents every 5 steps, followed by iterative refinement at each warping stage. We found t=15 is sufficient as the last iterative refinement step. The number of refinement iterations gradually decreases, starting from N=8 and reducing to N=3.

#### 4.2. Results

**Baseline Methods.** Since there are no direct competitors for zero-shot stereo video generation, we compare our method against different stereo conversion methods such as *ProPainter* (video inpainting), *RoDynRF* (novel-view synthesis), *ImmersePro* (stereo video conversion), and *Stere-*

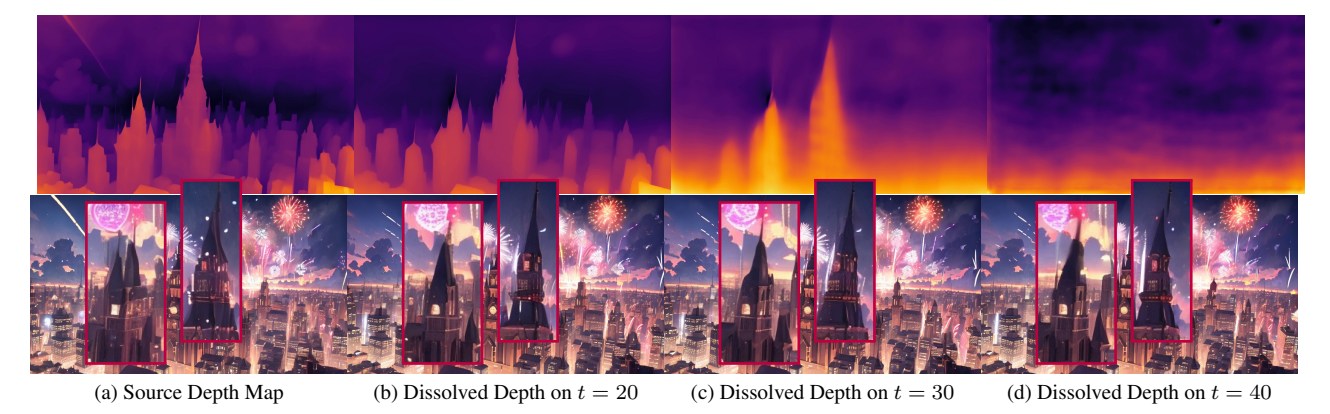


Figure 6. Dissolved depth maps obtained with DepthCrafter (50-step schedule). The top row shows the gradual removal of high-frequency details. The bottom row demonstrates ghosting effects reduction, but highlights a potential trade-off: increased distortion at larger t.

oDiffusion (stereo image generation). Note that *Immerse-Pro* is a depth-free method that may create an arbitrary degree of stereoscopic effect without the need for a depth map. For benchmarking purposes, we generated 40 video clips with *DynamiCrafter* spanning diverse domains such as anime, human subjects, animals, various objects, and imaginary contents. Note that generating one video clip with *RoDynRF* requires approximately 10 hours on an NVIDIA A100, we therefore neglected it in our benchmark tables but presented a visualization in Fig. 7.

Quantitative Results. Unlike stereo conversion, the stereo generation task lacks a ground-truth right view for direct comparison. Therefore, our evaluation focuses on two key aspects: semantic consistency and multi-view consistency between the left and right views of the generated video. For semantic consistency, we follow prior works in novel-view rendering [5, 6, 18], and report CLIP-based metrics [49] to compute the consistency between 1) the generated view and the text prompt (*CLIP-T*) and 2) the source-view videos and their corresponding generated views (*CLIP-F*). To evaluate the multi-view consistency, we employ MEt3R [1] to assess the epipolar consistency between the left and right views. We use *DINOv2* [25] as the feature extractor for MEt3R. Results in Tab. 5 show that our approach outperforms the baselines in both semantic multi-view consistency metrics.

	ProPainter ImmersePro StereoDiffusion			
CLIP-T↑	29.37	29.58	28.72	29.64
CLIP-F↑	96.45	96.99	91.09	97.16
MEt3R↓	8.82	5.69	6.09	4.95

Table 1. We measure text-image and semantic consistencies. Our method achieves the best results regarding the matching with the prompt and stereo videos.

**User Study.** To evaluate the quality of the generated videos, we conducted a user study involving 28 participants using a Meta Quest 3 headset. Each participant evaluated the qual-

ity of 5 selected videos generated by our method and other baseline methods. The results of this user study are summarized in Tab. 2, where our method achieved the highest overall user rating. Interestingly, while the inpainting-based method (*ProPainter*) presented slightly better stereo effects due to its enforcement of depth cues, it failed to maintain fine-grained details. In contrast, our method prioritizes overall harmonization, leading to an improved viewing experience, albeit with a minor trade-off in stereo effects. This balance between harmonization and depth accuracy was well-received by users.

	ProPainter	ImmersePro	StereoDiffusion	Ours
F.Q.	3.93	3.50	3.07	4.29
T.C.	3.93	3.64	2.79	4.07
S.E.	4.00	3.43	3.57	3.92
O.C.	3.93	3.64	3.29	4.29

Table 2. User study statistics of the preference rate for Frame Quality (F.Q.), Temporal Coherence (T.C.), Stereoscopic Effects (S.E.) and overall conformity (O.C.) of the stereo video.

Qualitative Results. In Fig. 7, we present visual comparisons against various competing methods, and stereo video examples are included in the supplementary material. The results show that our method consistently generates high-quality stereo videos, outperforming other approaches in terms of temporal coherence, resolution, and stereo effects. In addition, we visualize the effectiveness of our proposed modules in Figs. 8 and 9, showcasing their contributions to the overall video quality. We strongly encourage readers to watch the videos in the supplementary material, since temporal coherence and spatial jittering are hard to be fully appreciated in static images.

### 4.3. Evaluations

**Do Precise Depth Maps Matter?** As the essential ingredient for creating stereoscopic effects, depth information significantly affects the quality of the generated right views.

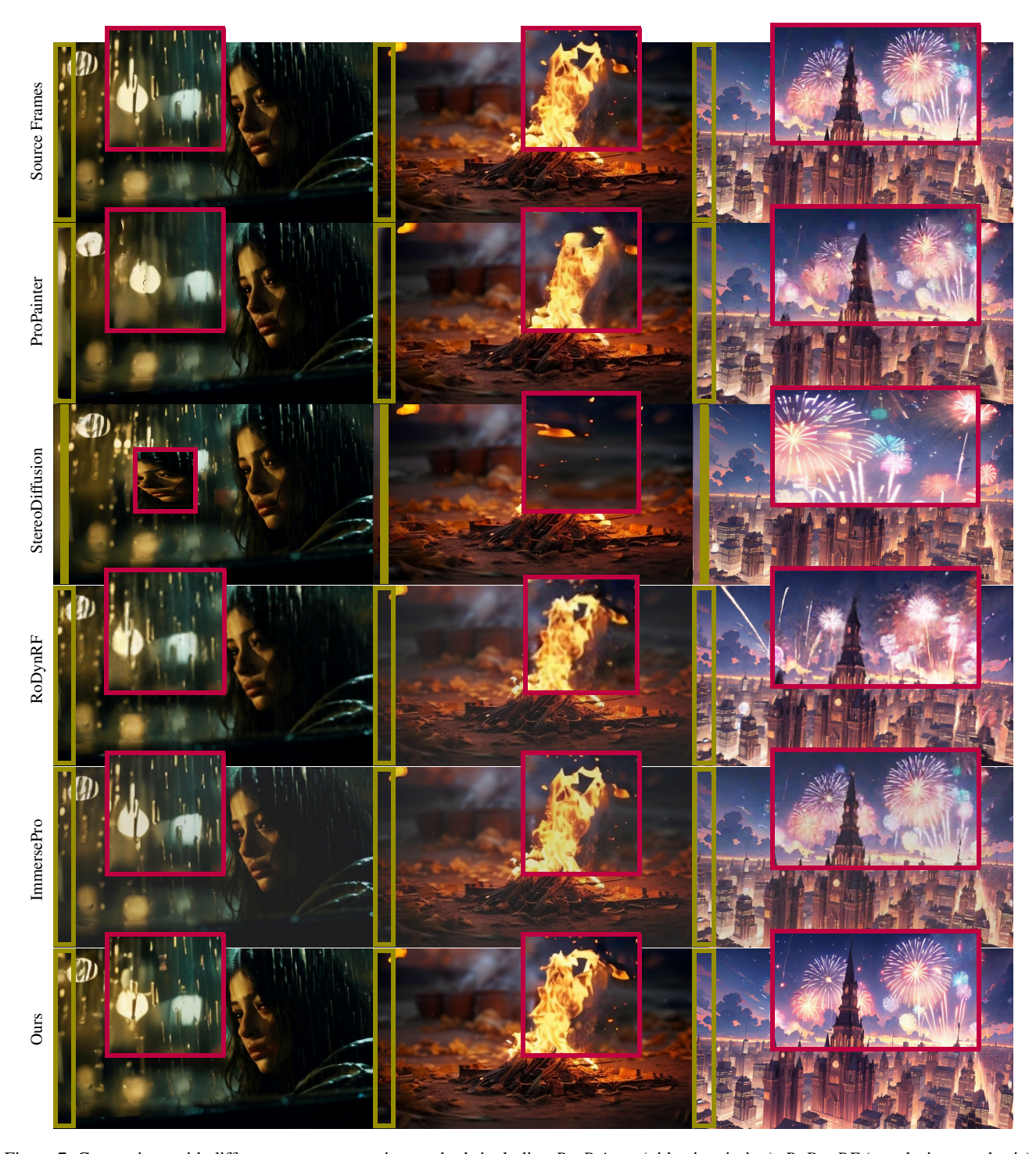


Figure 7. Comparison with different stereo conversion methods including *ProPainter* (video inpainting), *RoDynRF* (novel-view synthesis), *ImmersePro* (stereo video conversion), and *StereoDiffusion* (stereo image generation). The depth maps for those methods (if needed) are generated by *DepthCrafter*. Those methods mostly fail to handle the border properly. In addition, *ProPainter* can hardly handle the fine details such as rain drops and fire flames, *RoDynRF* can hardly maintain the scene structure correctly, *ImmersePro* may change the brightness of the scene, *StereoDiffusion* may produce more distortion since there are no temporal information constraints. We provide video demonstrations in our supplementary material.



Figure 8. Impact of the noisy restart on stereo effects. This analyph visualization vividly demonstrates the improvement. Increasing noisy restart iterations strengthens the stereo effects. Note: Results are achieved solely with noisy restart, without warping or iterative refinement.

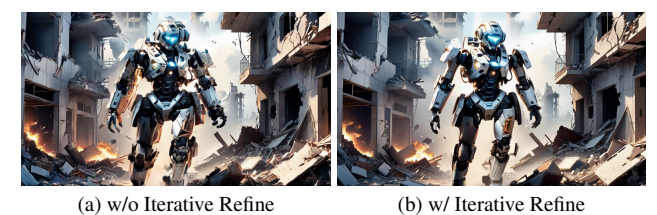


Figure 9. Impact of the iterative refinement. Without it, warping artifacts degrade the filling areas in later sampling stages. Iterative refinement ensures better consistency and handling of these areas.

Besides DepthCrafter, we evaluated our method using several state-of-the-art depth models, including Depth Pro [4], Depth Anything [41], and Video Depth Anything [9], to assess how depth estimation accuracy affects stereo generation. For image-based depth models, we applied a disparity propagation algorithm (see Appendix D.1 in supplementary) to enhance the temporal consistency. The statistical results in Tab. 3 show similar performances for different depth estimation models. A more detailed analysis is presented in the supplementary material.

	D. Pro	D. Anything	V. D. Anything	D. Crafter
CLIP-T↑	30.21	30.41	30.08	30.15
CLIP-F↑	97.92	98.02	97.92	98.04
CLIP-T↑ CLIP-F↑ MEt3R↓	6.78	6.71	6.79	6.70

Table 3. Performances obtained with different depth models.

How do dissolved depth maps help? We observe comparable performance across different SOTA depth models. As discussed in Sec. 3.3, high-frequency details in depth maps can disrupt latent space consistency during warping in diffusion models. To mitigate this issue, we proposed *dissolved depth maps*, which emphasize global structure to enhance consistency.

By experimenting with different levels of dissolving strength, we found that the optimal degree of dissolving depends on scene complexity. As shown in Tab. 4, for simpler scenes with fewer intricate structures, a stronger dissolving effect (t=40) produces better results. In contrast, for more complex scenes with fine textures and detailed depth varia-

tions, a weaker dissolving effect (t=20) is more effective, as it preserves critical structural details. We illustrate a representative case in Fig. 10, where dissolved depth maps can significantly reduce artifacts such as ghosting and jaggies. Additional results are provided in the supplementary.



(a) w/o Dissolved Depth

(b) w/ Dissolved Depth (t = 45)

Figure 10. Dissolved depth can effectively reduce the artifacts.

Dslv. Step	n/a	10	20	30	40
Simple Scene	8.59	8.78	8.94	8.67	<b>7.46</b> 4.93
Complex Scene	5.72	4.65	<b>4.37</b>	4.85	

Table 4. Impact of dissolving strength according to the scene complexity. Evaluation performed using MEt3R metric ( $\downarrow$ ).

# 5. Conclusion

In this work, we introduced StereoCrafter-Zero, a novel zero-shot stereo video generation approach. Stereo Crafter-Zero incorporates a noisy restart strategy for stereo-aware latent initialization and an iterative refinement process to enhance latent consistency by systematically injecting controlled noise. We also proposed dissolved depth maps that retains only low-frequency structural depth, reducing highfrequency noise and improving the coherence and stability of the stereoscopic effects. Our comprehensive evaluations, including statistical analysis and user studies, demonstrate the effectiveness of our method in generating high-quality stereo videos with enhanced depth consistency and temporal smoothness. Future research will focus on developing an adaptive method for determining the optimal dissolving level and exploring the incorporation of user guidance for personalized control over the generated stereo videos.

### References

- [1] Mohammad Asim, Christopher Wewer, Thomas Wimmer, Bernt Schiele, and Jan Eric Lenssen. Met3r: Measuring multi-view consistency in generated images. arXiv preprint arXiv:2501.06336, 2025. 6
- [2] Sherwin Bahmani, Ivan Skorokhodov, Victor Rong, Gordon Wetzstein, Leonidas Guibas, Peter Wonka, Sergey Tulyakov, Jeong Joon Park, Andrea Tagliasacchi, and David B. Lindell. 4d-fy: Text-to-4d generation using hybrid score distillation sampling. IEEE Conference on Computer Vision and Pattern Recognition (CVPR), 2024. 2
- [3] Jonathan T Barron and Jovan Popović. Structure-frommotion with oriented points. In *IEEE Transactions on Pattern Analysis and Machine Intelligence*, 2015. 2
- [4] Aleksei Bochkovskii, Amaël Delaunoy, Hugo Germain, Marcel Santos, Yichao Zhou, Stephan R Richter, and Vladlen Koltun. Depth pro: Sharp monocular metric depth in less than a second. arXiv preprint arXiv:2410.02073, 2024.
- [5] Shengqu Cai, Eric Ryan Chan, Songyou Peng, Mohamad Shahbazi, Anton Obukhov, Luc Van Gool, and Gordon Wetzstein. Diffdreamer: Towards consistent unsupervised single-view scene extrapolation with conditional diffusion models. In *Proceedings of the IEEE/CVF International Con*ference on Computer Vision, pages 2139–2150, 2023. 6
- [6] Shengqu Cai, Duygu Ceylan, Matheus Gadelha, Chun-Hao Paul Huang, Tuanfeng Yang Wang, and Gordon Wetzstein. Generative rendering: Controllable 4d-guided video generation with 2d diffusion models. In *Proceedings of* the IEEE/CVF Conference on Computer Vision and Pattern Recognition, pages 7611–7620, 2024. 6
- [7] Mingdeng Cao, Xintao Wang, Zhongang Qi, Ying Shan, Xi-aohu Qie, and Yinqiang Zheng. Masactrl: Tuning-free mutual self-attention control for consistent image synthesis and editing. In *Proceedings of the IEEE/CVF International Conference on Computer Vision*, pages 22560–22570, 2023. 1
- [8] Songyan Chen and Jiancheng Huang. Fec: Three finetuning-free methods to enhance consistency for real image editing. In 2023 International Conference on Image Processing, Computer Vision and Machine Learning (ICICML), pages 76–87. IEEE, 2023. 1
- [9] Sili Chen, Hengkai Guo, Shengnan Zhu, Feihu Zhang, Zilong Huang, Jiashi Feng, and Bingyi Kang. Video depth anything: Consistent depth estimation for super-long videos. arXiv preprint arXiv:2501.12375, 2025. 2, 8
- [10] Xi Chen, Lianghua Huang, Yu Liu, Yujun Shen, Deli Zhao, and Hengshuang Zhao. Anydoor: Zero-shot object-level image customization. In Proceedings of the IEEE/CVF Conference on Computer Vision and Pattern Recognition, pages 6593–6602, 2024. 1
- [11] Jaeyoung Chung, Suyoung Lee, Hyeongjin Nam, Jaerin Lee, and Kyoung Mu Lee. Luciddreamer: Domain-free generation of 3d gaussian splatting scenes. *arXiv preprint arXiv:2311.13384*, 2023. 2
- [12] Peng Dai, Feitong Tan, Qiangeng Xu, David Futschik, Ruofei Du, Sean Fanello, Xiaojuan Qi, and Yinda Zhang.

- Svg: 3d stereoscopic video generation via denoising frame matrix. arXiv preprint arXiv:2407.00367, 2024. 3
- [13] Jonathan Ho, Ajay Jain, and Pieter Abbeel. Denoising diffusion probabilistic models. In Advances in Neural Information Processing Systems, 2020. 2
- [14] Wenbo Hu, Xiangjun Gao, Xiaoyu Li, Sijie Zhao, Xiaodong Cun, Yong Zhang, Long Quan, and Ying Shan. Depthcrafter: Generating consistent long depth sequences for open-world videos. arXiv preprint arXiv:2409.02095, 2024. 2, 5
- [15] Jiancheng Huang, Yifan Liu, Jin Qin, and Shifeng Chen. Kv inversion: Kv embeddings learning for text-conditioned real image action editing. In *Chinese Conference on Pattern Recognition and Computer Vision (PRCV)*, pages 172–184. Springer, 2023. 1
- [16] Anant Khandelwal. Infusion: Inject and attention fusion for multi concept zero-shot text-based video editing. In Proceedings of the IEEE/CVF International Conference on Computer Vision, pages 3017–3026, 2023. 1
- [17] Johannes Kopf, Xuejian Rong, and Jia-Bin Huang. Robust consistent video depth estimation. In *Proceedings of the IEEE/CVF Conference on Computer Vision and Pattern Recognition*, pages 1611–1621, 2021. 2
- [18] Zhengfei Kuang, Shengqu Cai, Hao He, Yinghao Xu, Hong-sheng Li, Leonidas Guibas, and Gordon. Wetzstein. Collaborative video diffusion: Consistent multi-video generation with camera control. In arXiv, 2024. 2, 6
- [19] Zhengqi Li, Qianqian Wang, Forrester Cole, Richard Tucker, and Noah Snavely. Dynibar: Neural dynamic image-based rendering. In *Proceedings of the IEEE/CVF Conference on Computer Vision and Pattern Recognition (CVPR)*, pages 4273–4284, 2023. 2
- [20] Yu-Lun Liu, Chen Gao, Andreas Meuleman, Hung-Yu Tseng, Ayush Saraf, Changil Kim, Yung-Yu Chuang, Johannes Kopf, and Jia-Bin Huang. Robust dynamic radiance fields. In *Proceedings of the IEEE/CVF Conference on Computer Vision and Pattern Recognition*, 2023. 2
- [21] Xuan Luo, Jia-Bin Huang, Richard Szeliski, Kevin Matzen, and Johannes Kopf. Consistent video depth estimation. *ACM Transactions on Graphics (ToG)*, 39(4):71–1, 2020. 2
- [22] Lukas Mehl, Andrés Bruhn, Markus Gross, and Christopher Schroers. Stereo conversion with disparity-aware warping, compositing and inpainting. In *Proceedings of the IEEE/CVF Winter Conference on Applications of Computer Vision*, pages 4260–4269, 2024. 1
- [23] Chong Mou, Xintao Wang, Jiechong Song, Ying Shan, and Jian Zhang. Dragondiffusion: Enabling drag-style manipulation on diffusion models. arXiv preprint arXiv:2307.02421, 2023. 1
- [24] Jisu Nam, Heesu Kim, DongJae Lee, Siyoon Jin, Seungryong Kim, and Seunggyu Chang. Dreammatcher: Appearance matching self-attention for semantically-consistent text-to-image personalization. In *Proceedings of the IEEE/CVF Conference on Computer Vision and Pattern Recognition*, pages 8100–8110, 2024. 1
- [25] Maxime Oquab, Timothée Darcet, Théo Moutakanni, Huy Vo, Marc Szafraniec, Vasil Khalidov, Pierre Fernandez, Daniel Haziza, Francisco Massa, Alaaeldin El-Nouby, et al.

- Dinov2: Learning robust visual features without supervision. arXiv preprint arXiv:2304.07193, 2023. 6
- [26] Aditya Ramesh, Prafulla Dhariwal, Alex Nichol, Casey Chu, and Mark Chen. Hierarchical text-conditional image generation with clip latents. arXiv preprint arXiv:2204.06125, 1 (2):3, 2022. 2
- [27] Rene Ranftl, Katrin Lasinger, David Hafner, Konrad Schindler, and Vladlen Koltun. Towards robust monocular depth estimation: Mixing datasets for zero-shot cross-dataset transfer. *IEEE Transactions on Pattern Analysis and Machine Intelligence*, 44(3):1623–1637, 2022. 1
- [28] Robin Rombach, Andreas Blattmann, Dominik Lorenz, Patrick Esser, and Björn Ommer. High-resolution image synthesis with latent diffusion models. In arXiv preprint arXiv:2112.10752, 2022. 2
- [29] Jian Shi, Zhenyu Li, and Peter Wonka. Immersepro: End-to-end stereo video synthesis via implicit disparity learning. arXiv preprint arXiv:2410.00262, 2024. 2
- [30] Jian Shi, Pengyi Zhang, Ni Zhang, Hakim Ghazzai, and Peter Wonka. Dissolving is amplifying: Towards fine-grained anomaly detection. In *European Conference on Computer Vision*, pages 377–394. Springer, 2024. 5
- [31] Meng-Li Shih, Shih-Yang Su, Johannes Kopf, and Jia-Bin Huang. 3d photography using context-aware layered depth inpainting. In *IEEE Conference on Computer Vision and Pattern Recognition (CVPR)*, 2020. 1
- [32] Jaidev Shriram, Alex Trevithick, Lingjie Liu, and Ravi Ramamoorthi. Realmdreamer: Text-driven 3d scene generation with inpainting and depth diffusion. *arXiv preprint arXiv:2404.07199*, 2024. 2
- [33] Jingxiang Sun, Bo Zhang, Ruizhi Shao, Lizhen Wang, Wen Liu, Zhenda Xie, and Yebin Liu. Dreamcraft3d: Hierarchical 3d generation with bootstrapped diffusion prior. *arXiv* preprint arXiv:2310.16818, 2023. 2
- [34] Junshu Tang, Tengfei Wang, Bo Zhang, Ting Zhang, Ran Yi, Lizhuang Ma, and Dong Chen. Make-it-3d: High-fidelity 3d creation from a single image with diffusion prior, 2023. 2
- [35] Chaoyang Wang, Simon Lucey, Federico Perazzi, and Oliver Wang. Web stereo video supervision for depth prediction from dynamic scenes. In 2019 International Conference on 3D Vision (3DV), pages 348–357. IEEE, 2019. 1, 2
- [36] Lezhong Wang, Jeppe Revall Frisvad, Mark Bo Jensen, and Siavash Arjomand Bigdeli. Stereodiffusion: Training-free stereo image generation using latent diffusion models. In Proceedings of the IEEE/CVF Conference on Computer Vision and Pattern Recognition, pages 7416–7425, 2024. 2, 1
- [37] Jamie Watson, Oisin Mac Aodha, Daniyar Turmukhambetov, Gabriel J. Brostow, and Michael Firman. Learning stereo from single images. In European Conference on Computer Vision (ECCV), 2020. 1
- [38] Jamie Watson, Oisin Mac Aodha, Daniyar Turmukhambetov, Gabriel J Brostow, and Michael Firman. Learning stereo from single images. In Computer Vision–ECCV 2020: 16th European Conference, Glasgow, UK, August 23–28, 2020, Proceedings, Part I 16, pages 722–740. Springer, 2020. 1

- [39] Junyuan Xie, Ross Girshick, and Ali Farhadi. Deep3d: Fully automatic 2d-to-3d video conversion with deep convolutional neural networks. In Computer Vision–ECCV 2016: 14th European Conference, Amsterdam, The Netherlands, October 11–14, 2016, Proceedings, Part IV 14, pages 842–857. Springer, 2016. 1, 2
- [40] Jinbo Xing, Menghan Xia, Yong Zhang, Haoxin Chen, Wangbo Yu, Hanyuan Liu, Xintao Wang, Tien-Tsin Wong, and Ying Shan. Dynamicrafter: Animating open-domain images with video diffusion priors. arXiv preprint arXiv:2310.12190, 2023. 5
- [41] Lihe Yang, Bingyi Kang, Zilong Huang, Xiaogang Xu, Jiashi Feng, and Hengshuang Zhao. Depth anything: Unleashing the power of large-scale unlabeled data. *arXiv preprint arXiv:2401.10891*, 2024. 8
- [42] Heng Yu, Chaoyang Wang, Peiye Zhuang, Willi Menapace, Aliaksandr Siarohin, Junli Cao, Laszlo A Jeni, Sergey Tulyakov, and Hsin-Ying Lee. 4real: Towards photorealistic 4d scene generation via video diffusion models, 2024.
- [43] Wangbo Yu, Li Yuan, Yan-Pei Cao, Xiangjun Gao, Xiaoyu Li, Wenbo Hu, Long Quan, Ying Shan, and Yonghong Tian. Hifi-123: Towards high-fidelity one image to 3d content generation. *arXiv preprint arXiv:2310.06744*, 2023. 2
- [44] Wangbo Yu, Jinbo Xing, Li Yuan, Wenbo Hu, Xiaoyu Li, Zhipeng Huang, Xiangjun Gao, Tien-Tsin Wong, Ying Shan, and Yonghong Tian. Viewcrafter: Taming video diffusion models for high-fidelity novel view synthesis. *arXiv preprint arXiv:2409.02048*, 2024. 2
- [45] Haiyu Zhang, Xinyuan Chen, Yaohui Wang, Xihui Liu, Yunhong Wang, and Yu Qiao. 4diffusion: Multi-view video diffusion model for 4d generation. arXiv preprint arXiv:2405.20674, 2024. 2
- [46] Jingbo Zhang, Xiaoyu Li, Ziyu Wan, Can Wang, and Jing Liao. Text2nerf: Text-driven 3d scene generation with neural radiance fields. *IEEE Transactions on Visualization and Computer Graphics*, 2024. 2
- [47] Zheyu Zhang and Ronggang Wang. Temporal3d: 2d-to-3d video conversion network with multi-frame fusion. In 2022 4th International Conference on Advances in Computer Technology, Information Science and Communications (CTISC), pages 1–5. IEEE, 2022. 2
- [48] Sijie Zhao, Wenbo Hu, Xiaodong Cun, Yong Zhang, Xiaoyu Li, Zhe Kong, Xiangjun Gao, Muyao Niu, and Ying Shan. Stereocrafter: Diffusion-based generation of long and high-fidelity stereoscopic 3d from monocular videos. arXiv preprint arXiv:2409.07447, 2024. 2, 1
- [49] SUN Zhengwentai. clip-score: CLIP Score for Py-Torch. https://github.com/taited/clipscore, 2023. Version 0.1.1. 6

# StereoCrafter-Zero: Zero-Shot Stereo Video Generation with Noisy Restart

# Supplementary Material

### A. Preliminaries

Image Warping for Stereo View Synthesis Generating a stereo pair of a single input image includes warping the image based on a disparity map. The disparity map d can be computed using the depth map of the image:

$$d(x,y) = \frac{f \cdot B}{I_{depth}(x,y)},\tag{6}$$

where f is the focal length, B is an adjustable baseline distance, and  $I_{depth}(x,y)$  is the depth value for a pixel at the location (x,y). With the disparity map, the right-view image can be obtained by warping the original 2D image with:

$$I_{right}(x - d(x, y), y) = I(x, y). \tag{7}$$

This shift creates a horizontal parallax, mimicking the view-point difference. However, the warping operation requires a high precision of the depth map and can introduce artifacts and misalignments. Due to occlusions, some pixels in the right view may not have a corresponding pixel in the original image. Previous works [22, 37, 48] applied inpainting to handle the occluded and disoccluded areas.

Stereo Pair Generation with Diffusion Models. Recent works such as [36] propose to warp the latent space of an image diffusion model. This can be achieved since the early-stage sampling in diffusion models involves low-frequency signals that primarily define the contours of the generated image. When the step t is large, high-frequency signals in the later stage sampling refine the image details. Formally, the generative process for each DDIM step can be described as follows:

$$x_{t-1} = \sqrt{\alpha_{t-1}} \left( \frac{x_t - \sqrt{1 - \alpha_t} \epsilon_{\theta}^t(x_t)}{\sqrt{\alpha_t}} + \sqrt{1 - \alpha_{t-1} - \sigma_t^2 \epsilon_{\theta}^{(t)}(x_t)} + \sigma_t \epsilon_t, \right)$$

$$(8)$$

where  $\epsilon_t$  is noise following a standard Gaussian distribution  $\mathcal{N}(0,I)$ , independent of  $x_t$ , and  $\alpha_t$  controls the noise scale at step t with  $\alpha_0 := 1$ . As the only randomness during the diffusion process, we duplicate the  $\epsilon$  for different views by default in our work. Meanwhile, as demonstrated in Secs. 3.1 and 4, we found the noise level  $\epsilon$  plays an important role in creating stereoscopic effects.

Cross-View Attention To enhance multi-view consistency, many works [7, 8, 10, 15, 16, 23, 24, 36] modify the diffusion model's attention mechanism by replacing the query, key, and value pairs, ensuring coherent generation across different views. In this work, we allow the left view's query

(Q) to attend directly to the right view's key (K) and value (V). This mechanism promotes stronger alignment and coherence across views by sharing essential spatial and contextual information. Let  $Q_L, K_L, V_L$  and  $Q_R, K_R, V_R$  represent the query, key, and value matrices for the left view and right view, respectively. To align the right view with the left view's features, we use  $Q_L$  (from the left view) to attend to  $K_R$  and  $V_R$  (from the right view). Mathematically, the right view feature  $F_{R \to L}$  can be expressed as:

$$F_{R \to L} = \operatorname{softmax} \left( \frac{Q_L K_R^{\top}}{\sqrt{d}} \right) \cdot V_R.$$
 (9)

# B. An Efficient Warping Algorithm

We present a vectorization technique for efficiently implementing pixel-wise image transformations that involve pixel displacement maps. Traditional implementations of such transformations rely on nested loops to process each pixel individually, which can be computationally intensive and inefficient, especially for high-resolution images or large batches. Our method addresses these inefficiencies by leveraging advanced tensor operations in PyTorch to vectorize the computations while ensuring the correctness of the output, particularly in handling overlapping pixel assignments and maintaining the original assignment order.

**Problem Formulation.** Let  $I \in \mathbb{R}^{B \times C \times H \times W}$  be a batch of input images, where B is the batch size, C is the number of channels, and H and W are the height and width of the images, respectively. Let  $D \in \mathbb{R}^{B \times 1 \times H \times W}$  be the corresponding batch of depth maps or optical flow fields. The goal is to create a derived image I' by displacing pixels from the input image I based on the values in D, scaled by a factor s and an exponent a. This transformation can be formalized as:

$$I'_{b,c,h,w'} = I_{b,c,h,w}, \text{ where } w' = w + \text{offset}_{b,h,w},$$
 (10)

offset<sub>b,h,w</sub> = 
$$\left(D_{b,0,h,w}^{\alpha} \times s\right)$$
. (11)

The challenge arises when multiple source pixels (b,c,h,w) map to the same destination pixel (b,c,h,w'), leading to overlapping assignments. It is crucial to ensure that the final value of I' at any pixel (b,c,h,w') corresponds to the last assignment in the original processing order, consistent with the behavior of the nested loops.

**Baseline Implementation.** The traditional implementation uses three nested loops over the batch, height, and width dimensions:

for batch in range(B):

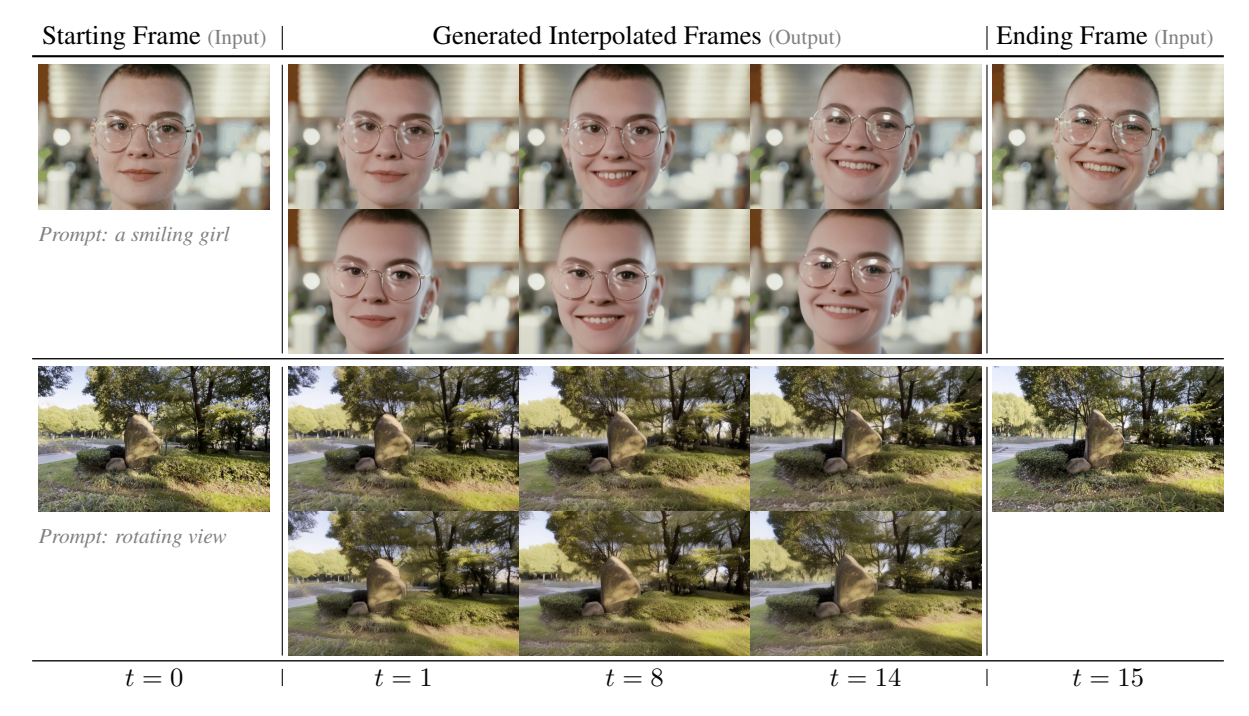


Figure 11. Demonstration of generating stereo videos with interpolated inputs. We input the starting and ending frames as our input and generate stereo content with our method. For each example, top row is the left view and bottom row is the right view.

This approach ensures correct handling of overlapping assignments by processing pixels in a specific order (e.g., from right to left when  $s \geq 0$ ) and overwriting previous values as needed. However, it is computationally inefficient due to the explicit loops.

Proposed Vectorization Technique. Our method eliminates the explicit loops by vectorizing operations across the batch, height, and width dimensions using PyTorch tensors. The key challenge is to replicate the assignment order of the nested loops to correctly handle overlapping assignments. First, we create tensors representing the batch, row, and column indices for all pixels. For positive movement such as  $s \ge 0$ , we process columns from right to left (W - 1 to 0), while we process columns from left to right (0 to W-1) for s < 0. For each column indices col, we then compute the offset D for each pixel and calculate the destination column indices  $col_d = col + D$ . Next, a Boolean mask is applied to filter out indices where  $col_d$  is outside the image boundaries. Note that the order for all valid indices is reversed to prioritize the last assignments in the original loop order. This conditional reversal ensures that, when duplicates are removed, the last assignment in the original loop order is preserved, correctly handling overlapping assignments. Next, we compute unique destination indices and keep the first occurrence, which corresponds to the last assignment due to reversal. We can then simply apply the computed index map to assign all pixels in bulk.

**Experimental Validation.** We validate our method by comparing the outputs and execution times of the original and vectorized implementations, as shown in Table 5. The values are computed with 20 executions for each run. The results show that our implementation offers an effective solution for efficiently implementing pixel-wise image transformations that involve displacement based on depth maps or optical flow fields.

Resolution	$128 \times 128$	$512 \times 512$
Baseline (ms) Ours (ms)	1401.18 1.47	22651.53 11.78

Table 5. Performance evaluation of our vectorized method for displacement handling. Our implementation speeds up the operation for 936 and 2022 times for the image resolution of 128 and 512, respectively.

# C. Additional Experiments

### C.1. Frame Interpolation And Looped Videos

Our method can be adapted to different video generation methods. We demonstrate generating stereo videos by us-

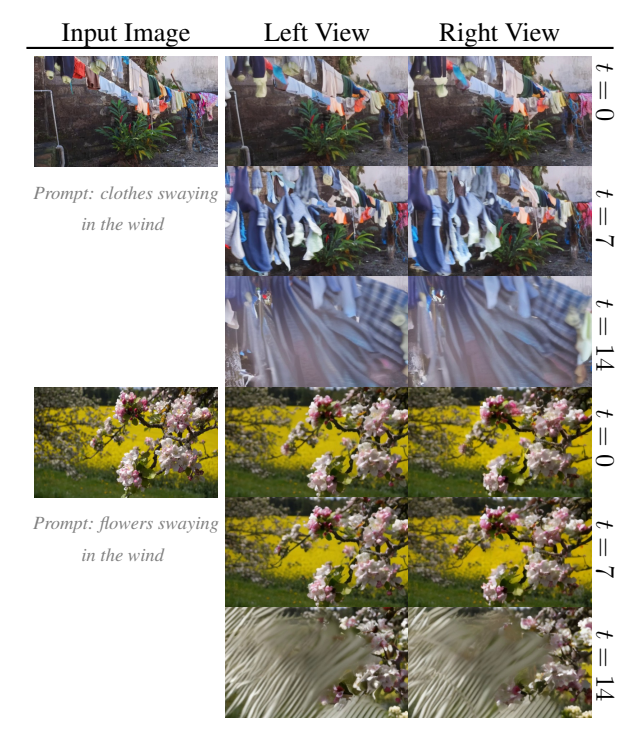


Figure 12. Demonstration of generating looped stereo videos. Starting with a single reference image, we produce a stereo video clip that seamlessly loops, offering visually continuous playback.

ing 1) frame interpolation, which generates stereo videos with a starting frame and an ending frame, and 2) looped videos, which generate a stereo video that keeps repeating without breaking the continuity. We present our generated videos in Figures 11 and 12. This video generation process operates under a stricter condition, wherein only the required frames are fixed, while all other frames are initialized to zeros. Our approach follows a similar configuration as outlined in the main text. In addition, once the results are obtained, we remove the fixed frame indices because such hard constraints can disrupt the smoothness and natural continuity of the generated videos. From our experiments, we observe that those hard constraints eliminate the stereoscopic effects on those frames. This step ensures a more coherent and visually appealing video output while adhering to the imposed frame constraints during the generation process.

### C.2. Failure Cases

The failure cases of our method can be categorized into two scenarios: 1) the diffusion model failed to generate meaningful videos from the provided conditions, and 2) the generated target view image does not align with the source view. Since the first scenario depends on the choice of the diffusion model, we only discuss the second scenario in this section. In general, our method may fail when a small ob-

ject moves with a strong motion. If the small object moves fast, the generated depth map may change rapidly while it may mess up the semantics of the latent space by the unnecessary intricate warping, resulting in a wrong interpretation of the depth and semantic information, as shown in Figure 13.

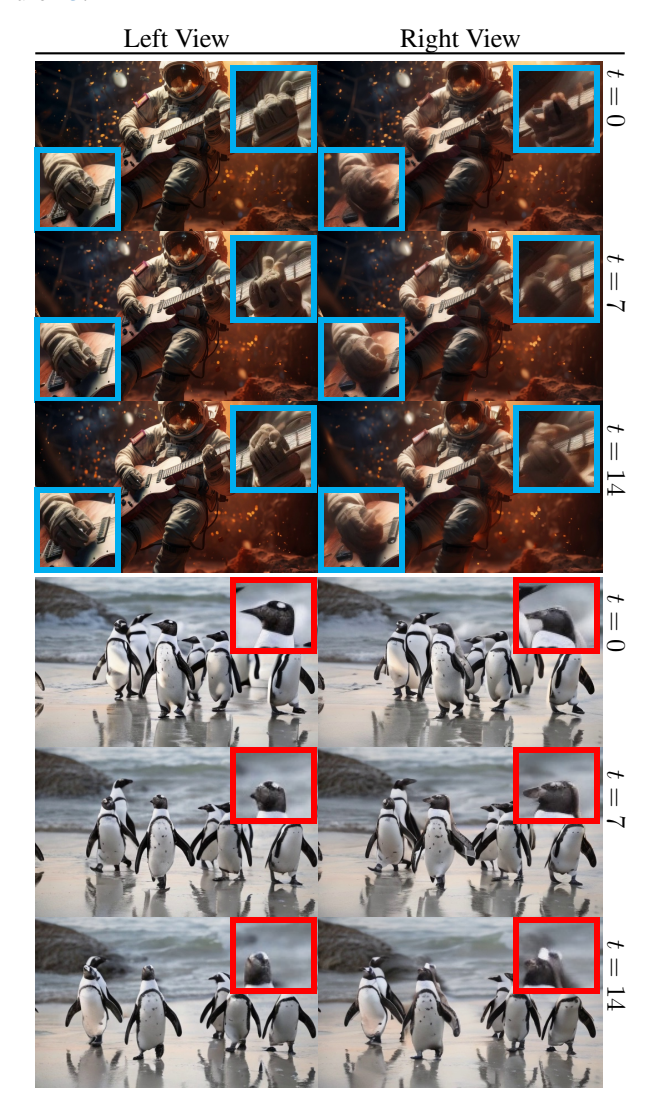
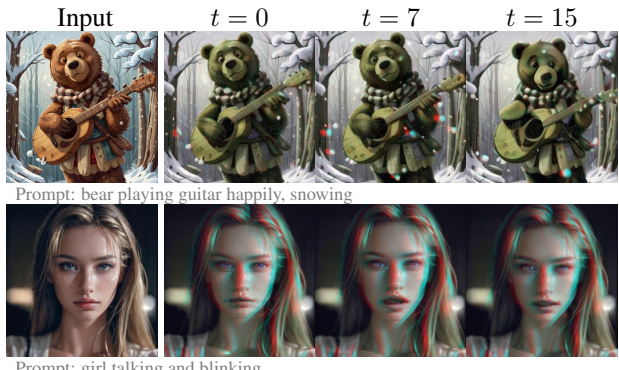


Figure 13. Demonstration of the failure cases. Our method can fail on the strong motion areas such as the rapid moving hand gesture and head pose.

### C.3. Multi-Resolution Support

Our method supports various resolutions, such as  $576 \times 1024$ ,  $320 \times 512$ , and  $256 \times 256$ . The images shown in our main text and supplementary materials are  $576 \times 1024$  and  $320 \times 512$  samples. In addition, we show  $256 \times 256$  samples in Figure 14 for demonstration purposes. By default, we recommend using dissolving strength of t=45 for  $576 \times 1024$  videos with 34 as the last warping step,



Prompt: girl talking and blinking

Figure 14. Demonstration of  $256\times256$  examples. Shown in analyph for visualizing the stereoscopic effect.

t=40 for  $320\times512$  videos with 44 as the last warping step. For  $256\times256$  resolutions, we found the dissolving is no longer required to obtain good results.

### C.4. A Pitfall in Latent Video Diffusion Models

Our method can be extended to other diffusion-based models. However, whilst experimenting with the naive latent video diffusion models (LVDMs), we found LVDMs can not handle repetitive patterns in the latent space properly. This can happen when inpainting the warped latent features with the source view latent. To further illustrate that, we experiment by applying affine transformation (*s.t.* translation) to the latent space with border padding. We can observe that the generated images are degenerated, as shown in Figure 15.



Figure 15. Warp LVDM latent space with direct translation with border padding on t=10. np denotes the number of rows of pixels that are shifted.

In our experiment, such an issue can be addressed by preventing the potential repetitive patterns, by inpainting with random Gaussian noises, or by our proposed noisy restart method (that uses both the source view latent and a small amount of random Gaussian noises). We show the improved results in Figure 16.

# D. Perfect Depth Maps Can Be Imperfect

This section introduces a disparity propagation approach that can generate depth maps with consistent depth values, then we compare this solution against the video depth estimation approach.



Figure 16. Demo of repetitive latent warping for LVDMs. Left: filling with source view (w/o repetitive patterns). Right: filling with random noise (w/ repetitive patterns).

### **D.1.** Disparity Propagation

With the aim of a more stable video with fewer artifacts, we first obtain a video depth map that allows smoother transitions and minimizes abrupt depth changes. Therefore, we propose *disparity propagation*, that propagates depth information from a single, initial depth frame across the entire video using frame-by-frame optical flow warping. This approach provides a smoother, more consistent disparity map over time, as it mitigates frame-specific artifacts by avoiding the per-frame recalculation of depth.

Given an initial depth map  $D_t$  for the frame at time t, we estimate the depth map at the previous t+1 frame and the next t-1 frame by warping  $D_t$  based on the forward and backward optical flow,  $F_{t \to t+1}$  and  $F_{t \to t-1}$ . We use a warping operation to apply the optical flow  $F_{t \to t+1}$  to adjust  $D_t$  based on the motion between the frames. The forward warping function can be expressed as:

$$D_{t+1}(x,y) = D_t(x + F_{t\to t+1}^x(x,y), \ y + F_{t\to t+1}^y(x,y)).$$
(12)

Note that the backward warping  $D_t$  to  $D_{t-1}$  can also be achieved with this operation since  $F_{t+1 \to t} = -F_{t \to t+1}$ . We repeat the process for each precedent and subsequent frame to propagate the initial depth across the entire video sequence. This produces a sequence of disparity maps  $S_D = \{D_0, D_1, \dots, D_T\}$  that are inherently smooth and consistent over time. In our work, we compute the disparity propagated depth maps for each frame, obtaining  $\{S_D^0, \dots, S_D^T\}$ . For each frame at time t, we take an average of  $\{S_D^0[t], \dots, S_D^T[t]\}$  as the final depth.

# **D.2. Disparity Propagation vs. Video Depth Esti-**mation

Existing video depth estimation models often overemphasize subtle scene movements, such as the drift of particles or minor background elements. Commonly, such objects are fine-grained high-frequency information that is not exhibited in the early stages of a diffusion latent representation. As shown in Figure 20, the early latent spaces mostly emphasize the low-frequency structure information.

The direct use of video depth estimation results may mistakenly warp the low-frequency latent component using the prediction of high-frequency depth maps. This can

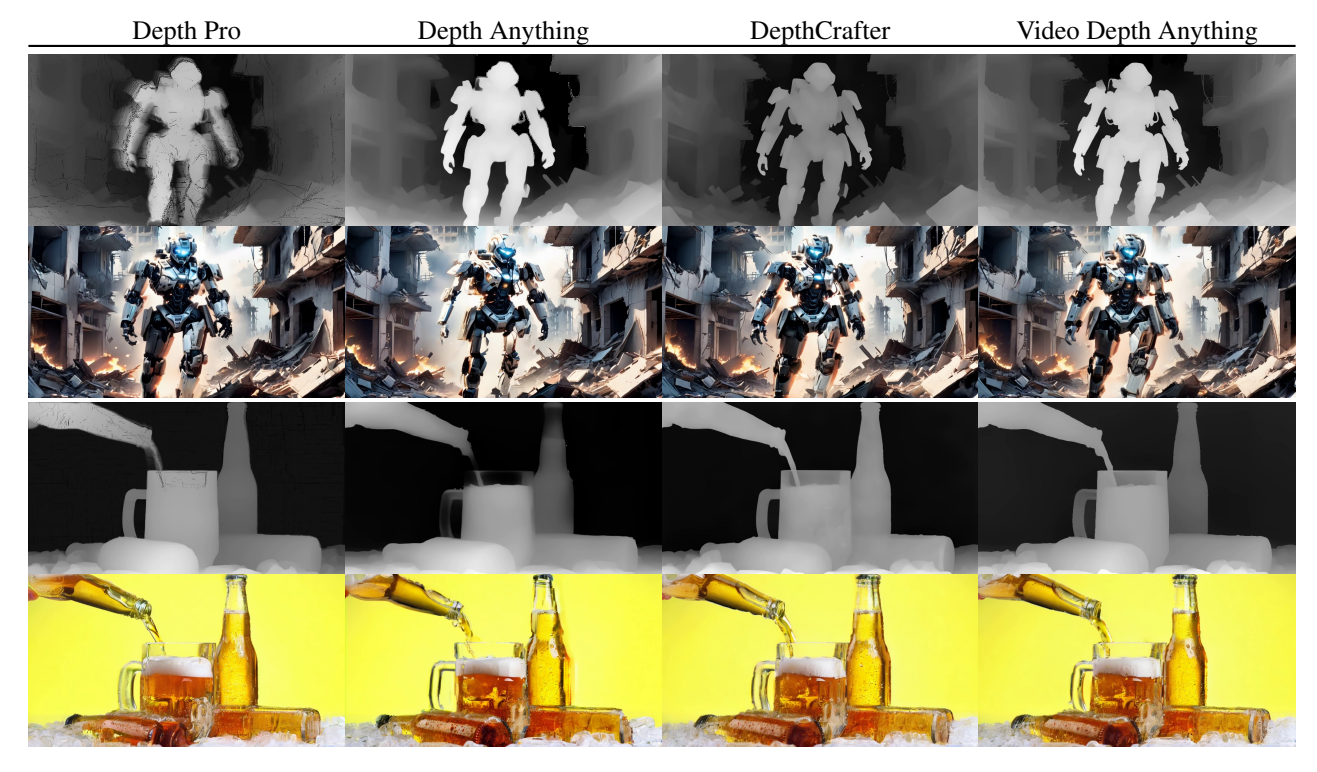


Figure 17. A cross comparison of depth maps from the disparity propagated image-based models and the video depth models. The visual quality indicates that the DepthPro may obtain a better performance.

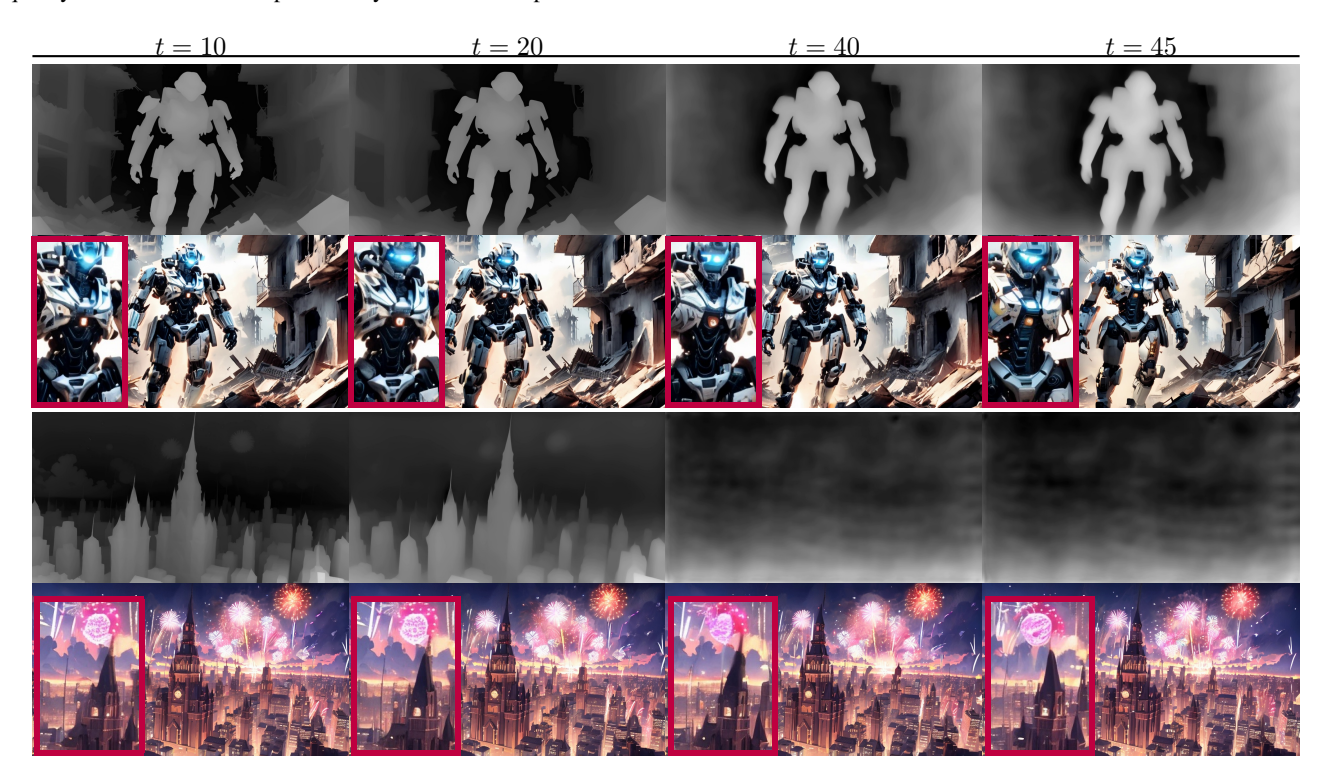


Figure 18. A cross comparison of different dissolving levels. Top: a simpler case with fewer intricate structures. Bottom: a complex case with fine textures and detailed depth variations.

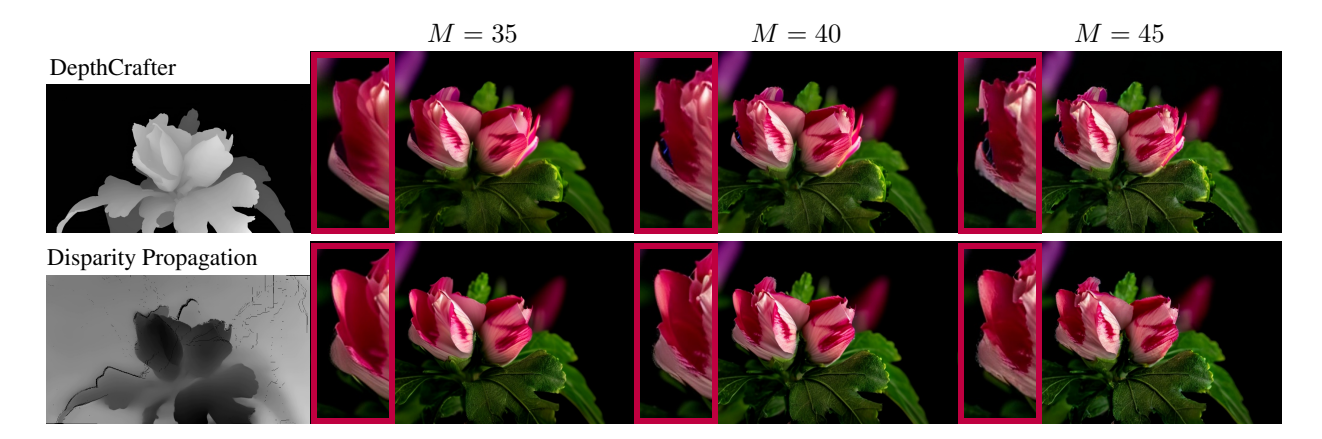


Figure 19. Demonstration of the differences between using DepthCrafter and Disparity Propagation method for obtaining disparity values. M denotes the early-stop sampling step for the warping operation. Both depth images and generated samples are taken from the  $12^{th}$  frame. We can see that DepthCrafter offers a better depth map but it may create sharp textures for a larger M while the disparity propagation method may mitigate such effects though a less accurate depth map provided.

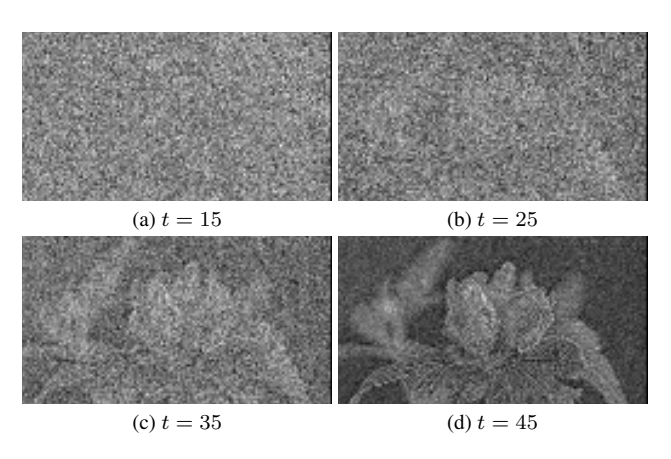


Figure 20. We visualize the tensor of the first timeframe in the first channel of the latent space of video diffusion. We can observe that the significant structural information does not show before t=25.

lead the model to assign high importance to irrelevant objects or minor details, which misleads the generation model into emphasizing non-crucial elements. Moreover, although these models generally produce consistent depth estimates across the scene, they occasionally introduce significant artifacts. For instance, objects may appear to shift abruptly from far to near within the frame, or objects ignored in previous frames may suddenly appear, leading to sudden jumps in perceived depth. Such inconsistencies can result in collapsed or distorted video generation. As shown in Figure 19, the depth map generated from a video depth estimator may mess up the border values due to the potential inconsistency around the edges, which is especially crucial for warping since the values may be moved to a wrong location.

In our current implementation, we still prefer a video

depth estimator since this depth propagation approach may fail to generate a meaningful disparity map to handle the scenarios that come with a strong motion. We demonstrate different disparity propagated depth and video depth estimation results in Fig. 17. However, supported by our aforementioned experiment, one potential solution might be employing a progressive depth map that can gradually increase the depth information for high-frequency objects. In the future, we believe a progressive depth map may further benefit the generation process.

# **D.3. Dissolved Depth Maps**

As mentioned in our main text, we found that the optimal degree of dissolving strength depends on scene complexity. For simpler scenes with fewer intricate structures, a stronger dissolving effect (t=40) produces better results whilst a weaker dissolving effect (t=20) is more effective for more complex scenes with fine textures and detailed depth variations. Here, we present some visual results to support this finding in Fig. 18.

# **D.4. Downsampling Depth Maps**

Apart from using dissolved depth maps, downsampling is another intuitive method to create depth maps in lower-

	). Pro	D. Anything	V. D. Anything	D. Crafter				
scale.				n/a	10	20	30	40
1   0	6.78	6.71	6.79	6.70	7.34	6.90	6.49	6.72
1/2   1/4   1	6.59 5.81	6.57 6.07	5.91 6.20	6.47 6.57	6.47 5.67	5.91 5.54	5.52 4.95	5.67 4.96

Table 6. Numerical results for different scales of the depth maps. We report MEt3R in this table.



Figure 21. A screenshot captured on Meta Quest 3, showcasing a 3D movie in action.

frequency. As shown in Tab. 6, having downsampled depth maps may generally create a better numerical results. However, the strengths of stereoscopic effects might be presented in a random manner for different videos.

# E. User Study

Our survey is designed with four questions for each method, such as:

- 1. Frame Quality (5 is best, 1 is poor)
- 2. Temporal Coherence (5 is best, 1 is poor)
- 3. Stereoscopic Effects (5 is best, 1 is poor)
- 4. Overall Conformity (5 is best, 1 is poor)

Specifically, we define frame quality as the quality of the generated 2D images, temporal coherence as the consistency between frames, and stereoscopic effects as a subjective experience of the stereo videos. For the overall conformity, while some stereo videos may exhibit stronger stereo effects, they can also induce discomfort or motion sickness in viewers. Therefore, the "overall conformity" reflects the subjective perception of our users regarding the generated videos.

The answer for each question is a radio of five integer values ranging from 1 to 5. Then each participant would watch our prepared videos on a Meta Quest 3 device. Figure 21 showcases a 3D movie being viewed through the headset. The study included 2 users who reported previous difficulty with 3D effects and 5 users who came with previous VR headset experiences.